

Something something something physics

Steven Green
of Emmanuel College

A dissertation submitted to the University of Cambridge
for the degree of Doctor of Philosophy

Abstract

This thesis describes the optimisation of the calorimeter design for collider experiments at the future Compact Linear Collider (CLIC) and the International Linear Collider (ILC). The detector design of these experiments is built around high-granularity Particle Flow Calorimetry that, in contrast to traditional calorimetry, uses the energy measurements for charged particles from the tracking detectors. This can only be realised if calorimetric energy deposits from charged particles can be separated from those of neutral particles. This is made possible with fine granularity calorimeters and sophisticated pattern recognition software, which is provided by the PandoraPFA algorithm. This thesis presents results on Particle Flow calorimetry performance for a number of detector configurations. To obtain these results a new calibration procedure was developed and applied to the detector simulation and reconstruction to ensure optimal performance was achieved for each detector configuration considered.

This thesis also describes the development of a software compensation technique that vastly improves the intrinsic energy resolution of a Particle Flow Calorimetry detector. This technique is implemented within the PandoraPFA framework and demonstrates the gains that can be made by fully exploiting the information provided by the fine granularity calorimeters envisaged at a future linear collider.

A study of the sensitivity of the CLIC experiment to anomalous gauge couplings that effect vector boson scattering processes is presented. These anomalous couplings provide insight into possible beyond standard model physics. This study, which utilises the excellent jet energy resolution from Particle Flow Calorimetry, was performed at centre-of-mass energies of 1.4 TeV and 3 TeV with integrated lumi-

nosities of 1.5ab^{-1} and 2ab^{-1} respectively. The precision achievable at CLIC is shown to be approximately one to two orders of magnitude better than that currently offered by the LHC.

Finally, a study into various technology options for the CLIC vertex detector is described.

Declaration

This dissertation is the result of my own work, except where explicit reference is made to the work of others, and has not been submitted for another qualification to this or any other university. This dissertation does not exceed the word limit for the respective Degree Committee.

Andy Buckley

Acknowledgements

Of the many people who deserve thanks, some are particularly prominent, such as my supervisor...

Preface

This thesis describes my research on various aspects of the LHCb particle physics program, centred around the LHCb detector and LHC accelerator at CERN in Geneva.

For this example, I'll just mention Chapter ?? and Chapter ??.

Contents

1	Capacitively Coupled Pixel Detectors for the CLIC Vertex Detector	1
1.1	Introduction	1
1.1.1	HV-CMOS	2
1.1.2	CLIC ASICs	4
1.1.3	Capacitive Coupling	6
1.2	Device Fabrication	6
1.3	Device Characterisation	8
1.3.1	Source Measurements	8
1.3.2	Test Pulse Calibration	15
1.4	Test Beam Analysis	21
1.4.1	Test Beam Setup	21
1.4.2	Analysis	22
1.4.3	Results	23
1.5	Conclusions	24
	Bibliography	27
	List of figures	33
	List of tables	37

*“Writing in English is the most ingenious torture
ever devised for sins committed in previous lives.”*

— James Joyce

Chapter 1

Capacitively Coupled Pixel Detectors for the CLIC Vertex Detector

“There, sir! that is the perfection of vessels!”

— Jules Verne, 1828–1905

1.1 Introduction

Identification of heavy-flavour quarks and tau-leptons at the linear collider experiment will rely upon precise reconstruction of secondary displaced vertices that are produced when these particles decay. Furthermore, the ability to accurately associate any daughter tracks produced in such decays, to the secondary vertices is essential. At the CLIC experiment this can only be realised using a vertex detector with a very high spatial resolution, of approximately $3\text{ }\mu\text{m}$, and good geometric coverage, extending to low θ values. The vertex detector must also have a low material budget (less than $0.2\text{ }X_0$ per layer) in order to prevent additional decay vertices from material interactions (CONFIRM!), and maintain a low occupancy, despite the high presence of beam-induced background particles. Low occupancy for the vertex detector will be achieved through the use of time-tagging, to an accuracy of 10 ns , to identify particles produced from the physics event of interest.

As there are currently no technology options that fulfil all of the criteria for the CLIC vertex detector, the CLIC experiment has developed an extensive R&D program where

new technologies for the vertex detector are considered. High-voltage complementary metal-oxide-semiconductor (HV-CMOS) sensors, which are capacitively coupled to a separate readout application-specific integrated circuit (ASIC) are one such option. The performance of prototype detectors based upon this technology and the impact of mechanical tolerances present in their manufacture are presented in this chapter.

1.1.1 HV-CMOS

Pixel detectors can be broadly classified in two groups: hybrid detectors, where a separate sensor and readout chip are bonded together; and fully-integrated devices, where the collection diode is implanted in the same piece of silicon as the readout circuitry. Fully-integrated devices have traditionally not been suitable for applications with tight timing requirements, due to relatively slow charge collection time and limited on-pixel functionality. However, recent developments in CMOS technologies, a method for constructing integrated circuits, have led to new assembly designs that may overcome some of these issues.

HV-CMOS is a processing technology whereby the n-MOS and p-MOS transistors forming the on-pixel electronics, are placed entirely within a deep n-well, as shown in figure 1.1. By varying the voltage applied at the gate terminal, n-MOS and p-MOS transistors are able to control the current flowing between the source and drain terminals. The gate voltage produces an inversion layer between the source and drain terminals that acts as a conduit allowing current to flow between the source and drain, as shown in figure 1.2. The voltage at the gate, with respect to the body, controls the width of the inversion layer and henceforth the magnitude of this current. Logic operations can be performed directly on-pixel using various configurations of the n-MOS and p-MOS transistors.

For the HV-CMOS, the deep n-well housing the on-pixel electronics acts as the charge collection diode as well as shielding the circuitry from the p-substrate. This shielding allows for the application of a moderate bias voltage to the sensor bulk that produces a depletion region, which facilitates fast charge collection via a drift current. In contrast, traditional monolithic active pixel sensors (MAPS) have a much smaller depletion region meaning charge collection occurs primarily through the slower mechanism of diffusion.

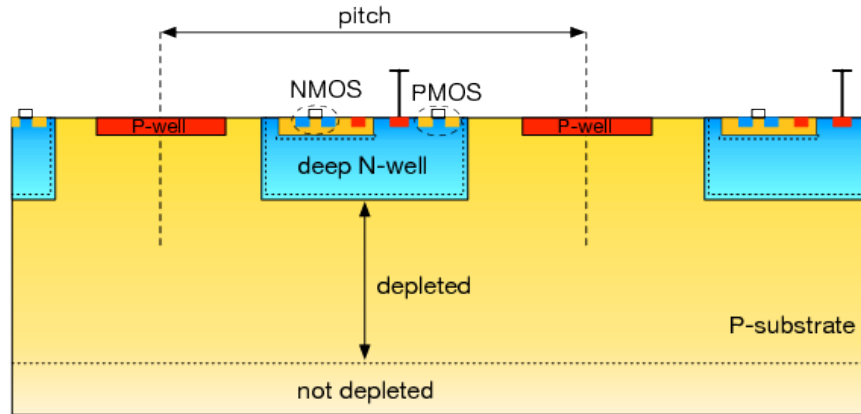


Figure 1.1: Schematic cross section of an HV-CMOS sensor: the deep n-well is the charge-collecting electrode and also contains additional CMOS circuits such as a preamplifier. Image taken from [3].

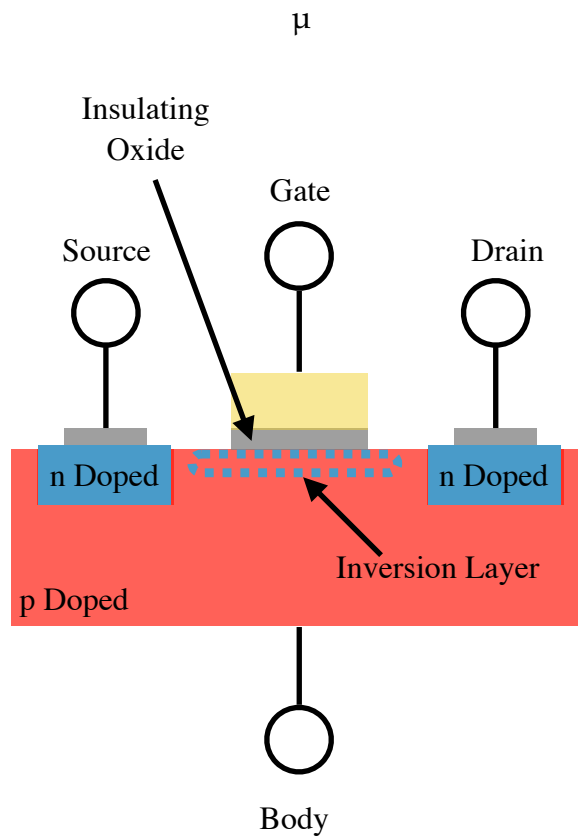


Figure 1.2: Schematic cross section of an n-MOS transistor. p-MOS transistors have a similar cross section where the n and p doped regions are switched.

Furthermore, in conventional MAPS there is potential for competition for charge collection between the n-well collecting diode and the p-MOS transistors used to perform logic operations as the p-MOS transistors are embedded within an n-well.

This only occurs as the n-well collection diode is separated from the n-wells housing the p-MOS transistors. The HV-CMOS technology does not suffer from this issue as the deep n-well collecting diode houses the p-MOS transistors meaning charge is only collected at a single well in the sensor bulk.

The HV-CMOS technology offers the possibility of fast charge collection with integrated on-pixel functionality, but several limitations still exist. As the on-pixel electronics have to be placed inside the deep n-well and the n-wells have to be separated from each other, there is a limited physical area of the pixel that can be used for the transistor layout, which limits the available on-pixel functionality. In addition to this, it is not possible to implement full CMOS logic inside the deep n-well as coupling between p-MOS transistors and the collection diode will lead to noise injection. While it is possible to embed p-MOS transistors within a p-well to shield them from the deep n-well, "quadruple-well technology", to give access to full CMOS logic this option is not readily available for prototyping. By restricting the complexity of on-pixel electronics and using a separate readout ASIC, it is possible to overcome many of these issues. When coupled with the fast charge collection time and removal of competition in charge collection this makes the HV-CMOS technology option highly desirable for use in the CLIC vertex detector.

1.1.2 CLIC ASICs

As the HV-CMOS technology is such a promising option for use at the CLIC vertex detector, prototype devices based on this technology have been developed for testing. Two ASICs have been developed: the charge coupled pixel device version 3 (CCPDv3), a sensor chip based on the HV-CMOS technology, and the CLICpix, a readout chip providing additional on-pixel logic operations. The pitch of the sensors, both the CCPDv3 and the CLICpix, produced for this study is 25 μm , which should be sufficient to meet the requirements for the CLIC vertex detector. Each of the prototype ASICs consists of a matrix of 64×64 pixels. A schematic of these devices can be found in figure 1.3.

CCPDv3

The construction of the CCPDv3 was done using a 65nm CMOS process. The 65 nm refers to the smallest size building blocks that can be used for creating the integrated

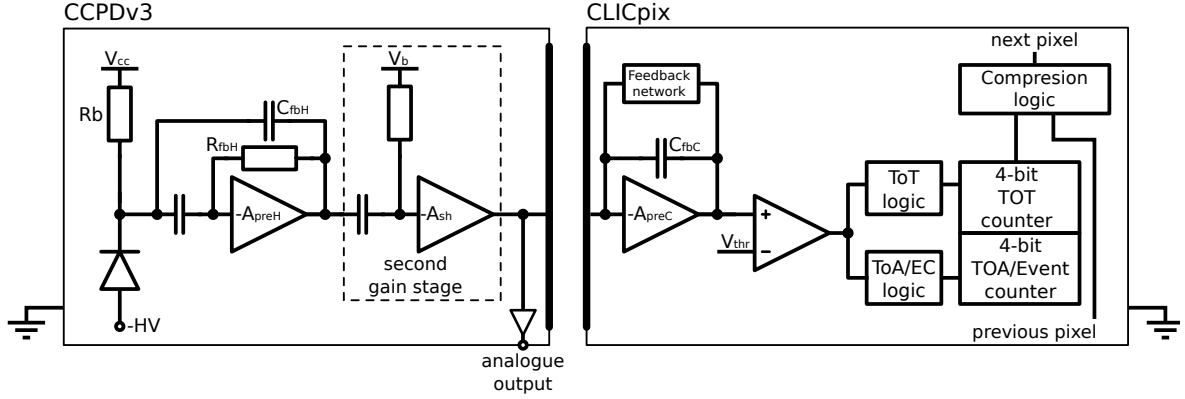


Figure 1.3: Schematic of CCPDv3 and CLICpix pixels.

circuits on a silicon wafer. This pushes the boundaries of semiconductor device fabrication for particle collider pixel detectors as current LHC experiments typically use 130 and/or 250 nm CMOS processes in the pixel detectors [1, 5]. This makes it possible to have more complex on-pixel circuitry incorporated into the CLIC vertex detector than would be possible in previous generations of pixel detectors.

CLICpix

The CLICpix is a hybrid pixel readout chip that has been developed for the CLIC vertex detector. Each CLICpix pixel contains a charge-integrating amplifier connected to a discriminator, as shown in figure 1.3. The discriminator fires for as long as the input signal is over a given threshold and this output is then used as the input for further logic operations. The additional logic operations record the time of arrival and magnitude of the collected charge, using a Time over Threshold (ToT) measurement. The ToT is stored in a 4-bit on-pixel counter.

The CLICpix operates using a shutter-based readout, where the entire matrix is kept active while the shutter is open and when closed the matrix is readout in its entirety. This is designed to match the expected beam structure for the CLIC experiment, as the accelerator will deliver bunch trains of e^+ and e^- that are separated by 20 ms. Each bunch train contains 312 bunches with a spacing of 0.5 ns, giving a total train length of 156 ns. Furthermore, the shutter-based readout is well suited to power-pulsing, whereby, the power to front-end electronics is turned off between bunch crossings. This helps to significantly reduce the power consumption of the pixel detector.

The threshold voltage, the voltage required for the discriminator to register an output, seen by each CLICpix pixel is slightly different, due to variations in the manufacturing process. If these variations are not accounted for then the behaviour of the device across the matrix will not be uniform. To minimise the impact of these fluctuations each CLICpix pixel contains a 4-bit local adjustment to the threshold voltage, which is calibrated to unify the response across the matrix. The threshold 'equalisation' is achieved by performing two threshold scans across the matrix, once with all four bits set to 0 (no local threshold adjustment), and a second time with all four bits set to 1 (maximum local threshold adjustment). For each scan, the baseline voltage of each pixel is determined. By applying a linear interpolation between the 0000 and 1111 cases, each pixel can be tuned to a common point, such that all pixels respond at the same global threshold.

1.1.3 Capacitive Coupling

Solder bump-bonding is the typical method used to connect sensor and readout ASICs in hybrid pixel detectors. This procedure uses small spheres of solder to connect each pixel on a sensor ASIC to the corresponding pixel on the readout ASIC. There are several drawbacks to the use of this procedure for pixel detectors: it is expensive and sets limits on the thickness of both ASICs that is required for mechanical stability. An alternative procedure for connecting the sensor and readout ASICs involves using a thin layer of glue to form a capacitive connection between the two. This procedure reduces the cost and material budget with respect to bump-bonding making it highly desirable for use at the CLIC vertex detector. However, as it has only recently been used to produce prototype devices, extensive tests have to be performed to determine whether this option is feasible. In order to make this procedure viable it is necessary to implement an amplifier in the CCPDv3 on-pixel logic, shown in figure 1.3, to boost the signal to overcome the intrinsically small capacitance of the gluing layer.

1.2 Device Fabrication

There are two issues related to device manufacture that have to be considered when using a capacitively coupled glue layer to connect the sensor and readout ASIC: the uniformity of the glue layer and the alignment of the sensor and readout pads. The

former has been investigated in [CERN FABRICATION NOTE CITE] while the latter is the focus of this study. In order to characterise the impact on detector performance of any misalignment between the CCPDv3 and the CLICpix pads, a number of pixel detectors have been constructed that purposefully contain misalignments, as shown in figure 1.4. Table 1.1 contains a summary of the samples produced.

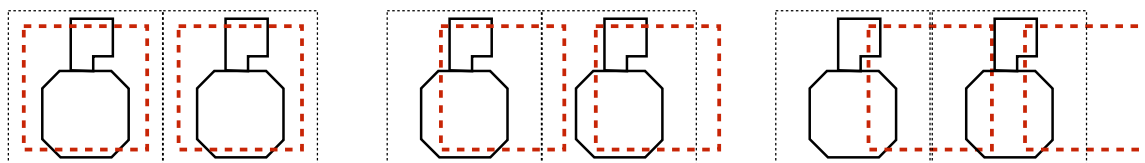


Figure 1.4: Alignment schematic of the CCPDv3 and CLICpix detectors studied. The red dotted line represents the CCPDv3 pad and the solid black line represents the CLICpix top metal layer. From left to right; centred pixels, 1/4 offset (6.25 μm) and 1/2 offset (12.5 μm).

Assembly	Alignment
SET9	Centred
SET10	$\frac{1}{4}$ Offset
SET12	Centred
SET13	Centred
SET15	Centred
SET16	$\frac{1}{2}$ Offset

Table 1.1: A list detailing the alignment of the CCPDv3 and CLICpix coupling pads for the devices considered in this study.

The full details of the glueing procedure can be found in [CERN FABRICATION NOTE CITE], along with a study of the absolute precision of the manufacturing procedure. For devices constructed in an identical fashion to those considered here, the glue layer thicknesses were less than 1 μm and the precision on the pad positioning was less than 0.5 μm . The reported pad positioning precision is sufficiently small that devices could be constructed with 1/4 offset and 1/2 offset with confidence.

1.3 Device Characterisation

A series of lab experiments were used to characterise the devices produced for this alignment study. Furthermore, the devices were also tested in realistic experimental conditions using the CERN SPS test beam. Due to the complexities of testing devices in a test beam, extensive lab test were performed first to characterise as many properties of the assemblies as possible. The lab experiments performed were as follows:

- **Radioactive source measurements.** The goal of this measurement is to measure the response of the CCPDv3 and CLICpix when using a radioactive source is used to deposit charge within the CCPDv3 sensor.
- **Test pulse calibration of the CLICpix chip.** The goal of this measurement is to calibrate the response of the CLICpix sensor. This is achieved by examining the CLICpix response when injecting a voltage pulse of fixed height directly into the input of the chip, which bypasses the CCPDv3 and glue layer.

1.3.1 Source Measurements

A radioactive source was used to deposit charge within the CCPDv3 sensor and the response of the CCPDv3 and CLICpix examined. The CCPDv3 sensor converts the deposited charge into a voltage, which in turn passes through the capacitively coupled glue layer and into the CLICpix chip. Measurements were made of the output voltage produced by the CCPDv3 and the response of the CLICpix readout chip, in units of ToT. As the exact amount of charge deposited by the radioactive sources is unknown, calibration of the CCPDv3 is not possible in this experiment. Instead, this experiment focuses on examining the shape of the voltage produced by the CCPDv3 and determining the response of the CLICpix chip as a function of this voltage. As the CCPDv3 signal passes through the capacitively coupled glue layer before entering the CLICpix chip, this experiment characterises the behaviour of the gluing layer as well as the sensor and readout chips.

Experimental Setup

The radioactive material used in this experiment was a Sr^{90} . Sr^{90} undergoes β^- decay to form Y^{90} , which in turn undergoes β^- decay to form the stable isotope Z^{90} . Each β^-

decay produces an e^- and a $\bar{\nu}_e$, and it is the e^- that goes on to deposit charge in the CCPDv3 sensor. The Sr^{90} source used for this experiment had an activity of 29.6 MBq.

The radioactive source was positioned directly above the back-side of the CCPDv3 sensor, and measurements were made of both the ToT output from the CLICpix and the CCPDv3 analogue signal for individual pixels on the sensor. The CCPDv3 pulse shape was recorded on a fast sampling oscilloscope that was also used to trigger the CLICpix readout. The on-pixel event counter, which is located in the CLICpix chip, was used to veto events where multiple hits occurred within the active shutter period. The CCPDv3 sensor was biased to 60 V during this experiment. Examples of CCPDv3 output voltage pulses when using the Sr^{90} source can be seen in figure 1.5. The analogue output has a baseline voltage of ≈ 1.15 V, with signal saturation occurring around a height of 700 mV.

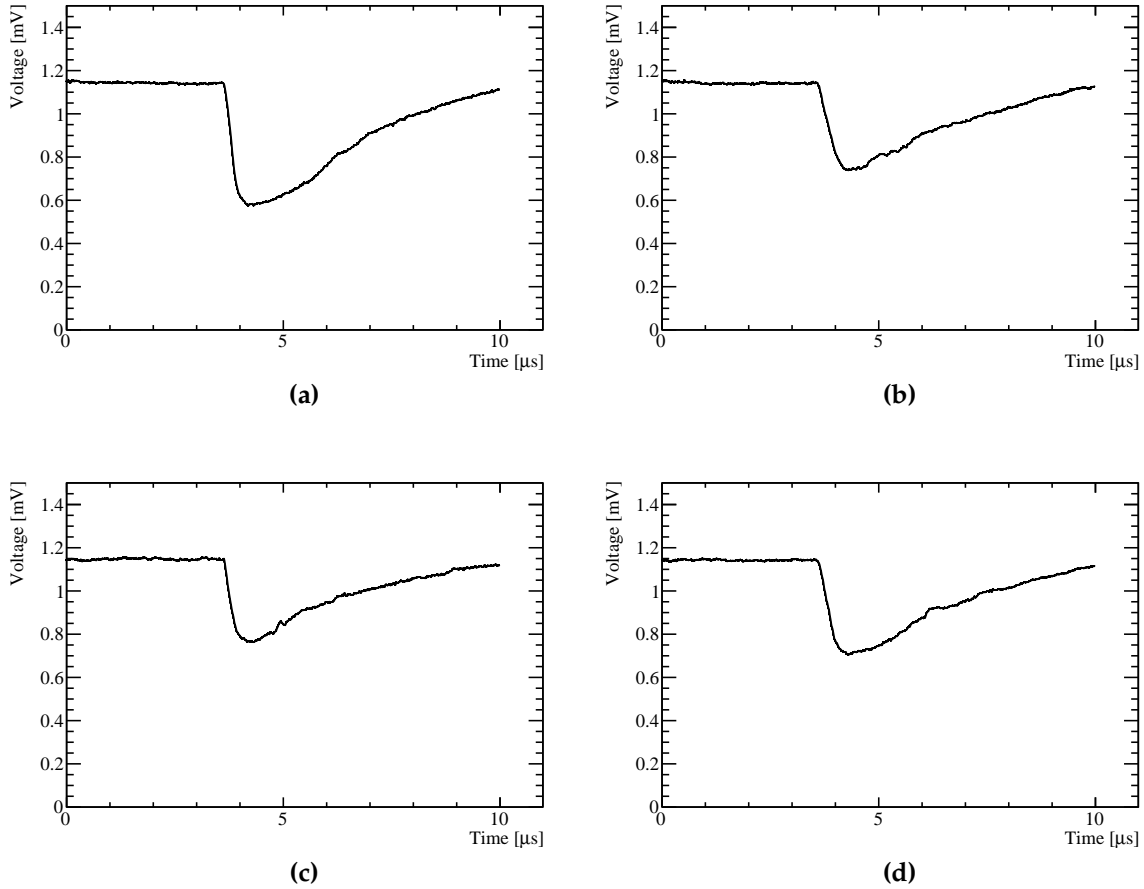


Figure 1.5: CCPDv3 voltage pulses produced using a radioactive source, Sr^{90} , to deposit charge in the sensor.

Analysis

The quantities of interest related to the CCPDv3 output voltage are the pulse height, defined as the peak of the voltage pulse, and the rise time, defined as the time it takes for the CCPDv3 to reach the pulse height. For ease of analysis the baseline voltage is subtracted from the CCPDv3 output voltage and the pulse shape inverted before the following analysis is applied to extract the variables of interest.

The pulse height is defined using a Gaussian fit to the peak of the voltage pulse. This method is used to minimise the dependency of the pulse height on small fluctuations in the output voltage. The peak of the voltage pulse is defined as the region where the change in the CCPDv3 voltage output is greater than 90% of the maximum change in the CCPDv3 voltage output.

The rise time is defined as the time taken for the signal to go from 10% to 90% of the maximum change in the CCPDv3 voltage output. This definition makes the rise time metric more robust against fluctuations in the CCPDv3 voltage output.

Examples of the calculation of these metrics for a representative pulse is shown in figure 1.6. Due to the design of the CCPDv3 matrix, it is only possible to record the CCPDv3 voltage output for 15 pixels running along one edge of the 64×64 matrix. Therefore, in the subsequent analysis data was taken for each of these accessible pixels and combined.

Results - Rise Time vs Pulse Height

The mean rise time as function of pulse height for the CCPDv3 output voltage is shown in figure 1.7. This was determined by binning the measurements in pulse height and determining the mean rise time for measurements in each bin. The pulse height was binned using a bin width of 4 mV ranging from 0 to 700 mV. A minimum of 10 measurements per bin were used for the calculation of the average rise time. The error bars on this figure show the standard error in the mean rise time. Data was only included in this analysis if the on-pixel event counter registered a single hit in the time window used to take data.

The data in figure 1.7 shows that the rise time for the CCPDv3 front-end is approximately 300 ns across all samples. The rise time is largely independent of pulse height for all but the smallest signals. For very small pulse heights (< 100 mV) rise times

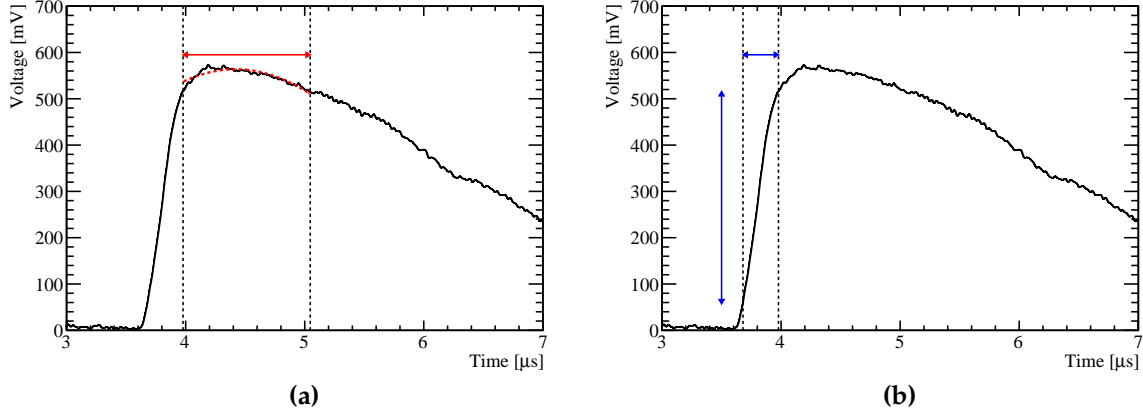


Figure 1.6: An example calculation of the pulse height and rise time for the CCPDv3 output voltage. In this example the black line show the CCPDv3 output voltage as a function of time where the baseline voltage has been subtracted and the pulse shape inverted. These voltage pulses were created using a radioactive source, Sr^{90} , to deposit charge in the sensor. (a) The definition of the pulse height. Pulse height is defined as the amplitude of a Gaussian function fitted across the peak of the voltage pulse. The peak of the voltage pulse is defined as the region where the voltage in excess of 90% of the raw pulse height, which is indicated in the figure by the red arrow. The red dotted line shows the Gaussian fit used to extract the pulse height. (b) The definition of rise time. Rise time is defined as the time taken for the CCPDv3 voltage to rise from 10% to 90% of the raw pulse height. The rise time, and change in CCPDv3 output voltage over this time, are shown in the figure by the blue arrows.

are significantly larger, which suggests that the deposited charge takes a longer time to be collected. This may be due to charge transport occurring via diffusion rather than drift. A gradual reduction in the rise time is observed as the total deposited charge, which is proportional to the pulse height, increases. This is expected as larger charge deposits in the sensor bulk lead to a greater the rate of charge collection by the CCPDv3 and a smaller time taken for the pulse height to reach the peak. As the intrinsic performance of the CCPDv3 sensors in the devices tested is very similar, comparisons of the misaligned samples will be made more straightforward. As nearly identical intrinsic performance was observed for the CLICpix readout chips, as will be shown in section 1.3.2, any performance differences observed between these devices will be entirely due to the capacitively coupled glue layer and the pad alignment.

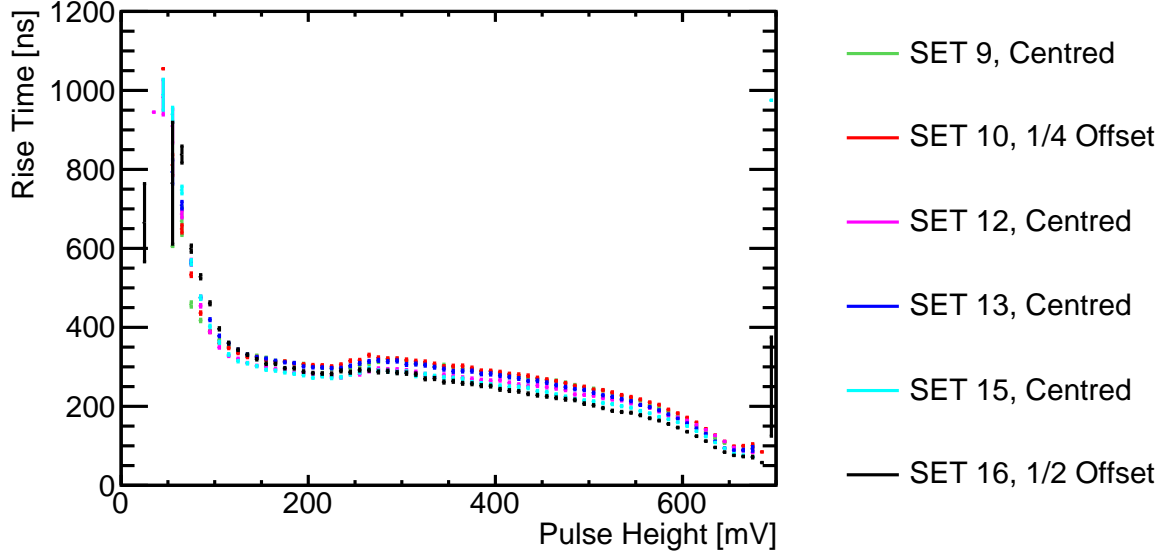


Figure 1.7: The CCPDv3 output voltage rise time as a function of pulse height.

Results - ToT vs Pulse Height

The mean ToT measured in the CLICpix as a function of the CCPDv3 output voltage pulse height is shown in figure 1.8. Determination of the mean and error bars for the ToT as a function of pulse height measurement is identical to that described above for the rise time as a function of pulse height measurement.

For samples where the CCPDv3 and CLICpix are centred, the distribution of the mean ToT against pulse height shows that the ToT increases with pulse height up to values of approximately 400 mV and for larger pulse heights the mean ToT saturates at ≈ 15 . It is expected that the $\frac{1}{4}$ - and $\frac{1}{2}$ -offset samples will have a lower ToT than the centred samples due to the lower effective capacitance between the CCPDv3 and CLICpix pads. The greater the offset, the smaller the effective capacitance to the target CLICpix pad will be, and so the lower the recorded ToT. This can be seen when comparing the centred samples to SET 10, the $\frac{1}{4}$ -offset sample, and SET 16, the $\frac{1}{2}$ -offset sample. In addition to the charge injected by the radioactive source there will also be background noise present from a variety of effects such as manufacturing defects in the silicon and thermal noise. This additional charge will increase the mean ToT recorded by the CLICpix and is the most likely reason as to why the mean ToT does not smoothly tend to zero as the pulse height decreases.

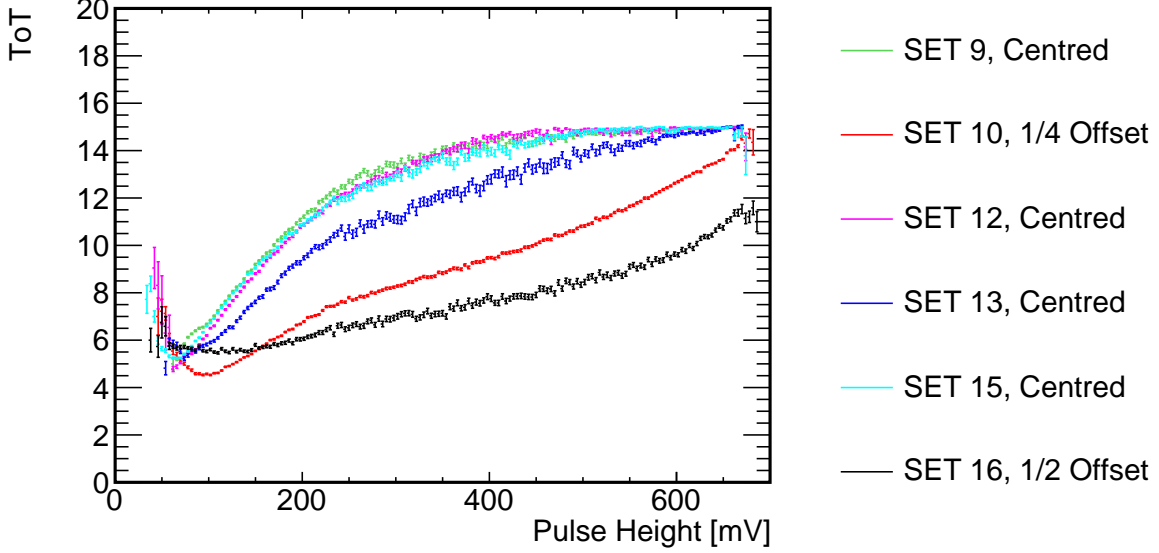


Figure 1.8: The mean ToT measured on the CLICpix ASIC as a function of CCPDv3 voltage pulse height.

Results - Cross Couplings

Capacitive coupling between a sensor and readout ASIC in a pixel detector can lead to the unwanted effect of cross-coupling. Cross-coupling is the transfer of signal from a sensor pad to the readout ASIC on an adjacent pad, which will occur if there is a non-negligible capacitance between the two pads. Signals are still transferred between the aligned sensor and readout pads, however, if the cross-capacitance is large enough unwanted additional hits in the neighbouring pads will be created. This issue is particularly relevant for this study as any misalignment between the sensor and readout pads will result in an increase in the cross-capacitance along the direction of the misalignment.

Any effects of cross-coupling can be studied using the same setup as was used in section 1.3.1 for the ToT against pulse height analysis, but by considering the ToT on the adjacent CLICpix pixel along the direction of the misalignment. The mean ToT on the adjacent pixel is shown as a function of the pulse height for all devices where the CCPDv3 and CLICpix are aligned in figure 1.9a and for the misaligned samples in figure 1.9b.

The distributions of the mean ToT on the adjacent CLICpix as a function of pulse height will be governed by two effects: cross-coupling and background noise. Cross-

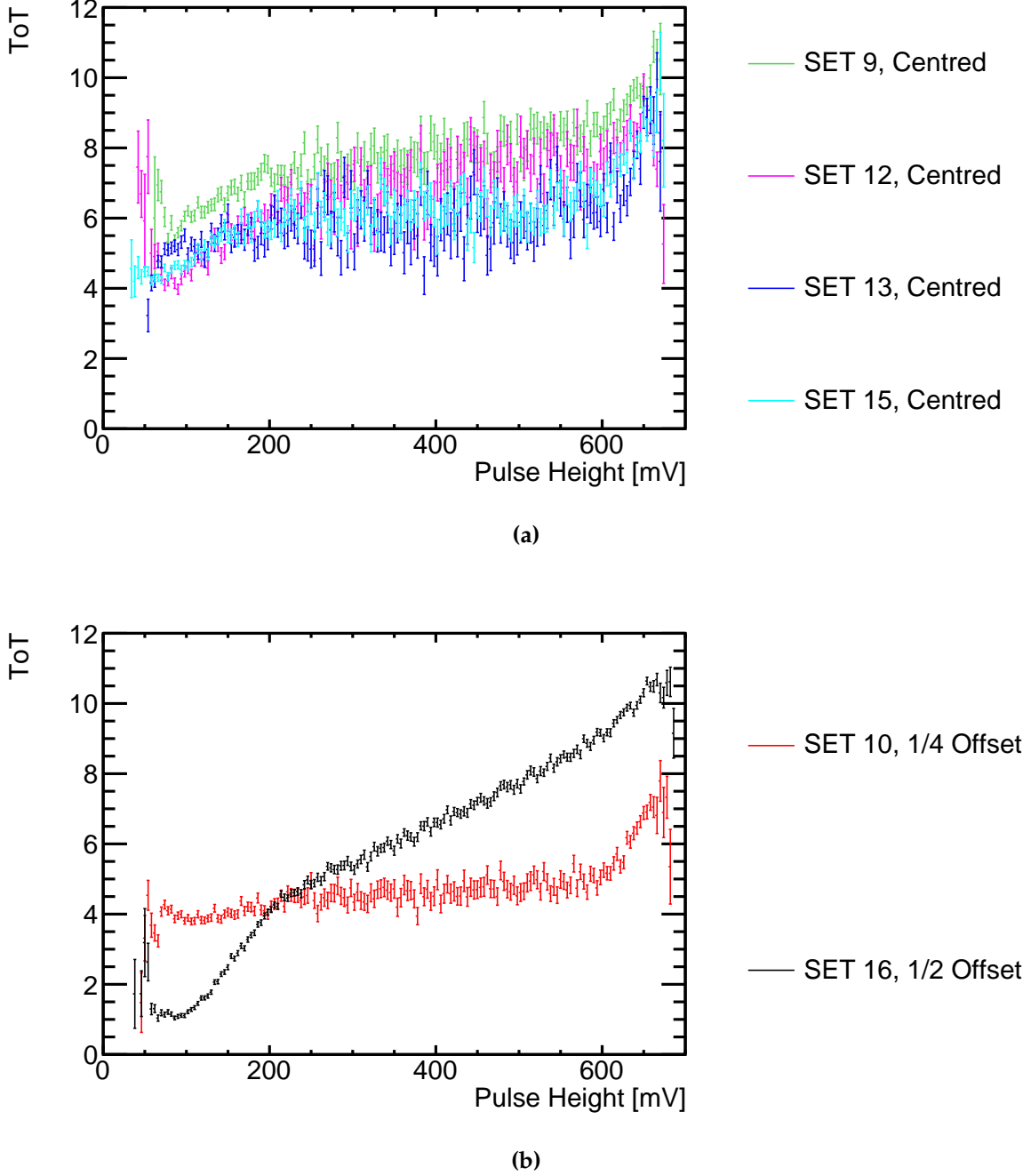


Figure 1.9: The mean ToT measured on the adjacent CLICpix pixel, along the direction of the offset, as a function of CCPDv3 voltage pulse height for (a) the centred and (b) the misaligned devices.

coupling effects will make this distribution look similar in shape to that of the mean ToT in the target CLICpix as a function of pulse height, shown in figure 1.8. However, the gradient of the adjacent ToT distribution will be shallower than the adjacent ToT

distribution as the cross-capacitance is smaller than the aligned capacitance. The exception to this is the $\frac{1}{2}$ -offset sample where the cross-capacitance and aligned capacitance will be comparable. The background will again act to offset the mean ToT by a fixed amount.

For the centred samples, the width of the mean of the adjacent ToT distribution is broader than that of the target ToT distribution, which can be seen when comparing the size of the errors in figures 1.8 and 1.9. This indicates that fluctuations in the background are dominating the adjacent ToT measurement for the centred samples and that cross-coupling is having a small effect. However, for the $\frac{1}{4}$ -offset sample the width of the adjacent ToT distribution is tighter than that of the centred samples, which indicates that the ToT measurement is less dominated by the background and more so by cross-coupling effects. An even stronger cross-capacitive effect can be seen in the $\frac{1}{2}$ -offset sample where the adjacent ToT distribution almost mirrors the aligned ToT distribution in terms of both shape and width of the distribution. There are some small differences between the shape of the aligned and adjacent ToT vs pulse height distribution for the $\frac{1}{2}$ -offset sample, which are understood to be from the column structure of the CLICpix readout ASIC, more details of which can be found in section 1.3.2. Overall, these results indicate that, as expected, the misalignment of between the CCPDv3 and CLICpix pads increases the effect of cross-coupling along the direction of the misalignment.

1.3.2 Test Pulse Calibration

In order to fully understand charge transfer to the CLICpix, a calibration of the CLICpix front-end electronics response was performed. This was achieved by directly injecting a voltage pulse of fixed height directly into a capacitor help in each CLICpix pixel. The voltage pulse will deposit a known amount of charge and by varying the height of the pulse applied the response of the CLICpix to different amounts of charge can be quantified. This experiment extends the characterisation of the CLICpix chip beyond what was found using the radioactive source measurements as applying the voltage directly to the CLICpix it fully isolates the response of the chip from any effects relating to the glue layer or CCPDv3.

Experimental Setup

To prevent any influence from neighbouring pixels during the testpulse measurements the matrix was pulsed in stages. Charge was injected into 1 out of every 16 pixels while masking the others to ensure issues related to power consumption were not encountered. This was repeated 15 more times using different mask configurations until the entire matrix had been sampled. This procedure was repeated 100 times to determine the average ToT response on a per-pixel level. The pulse height injected into the CLICpix was varied from 2 to 180 mV in steps of 2 mV in order to fully characterise the response up to saturation of the ToT output. An example of the mean ToT plotted against the injected pulse height is shown in figure 1.10.

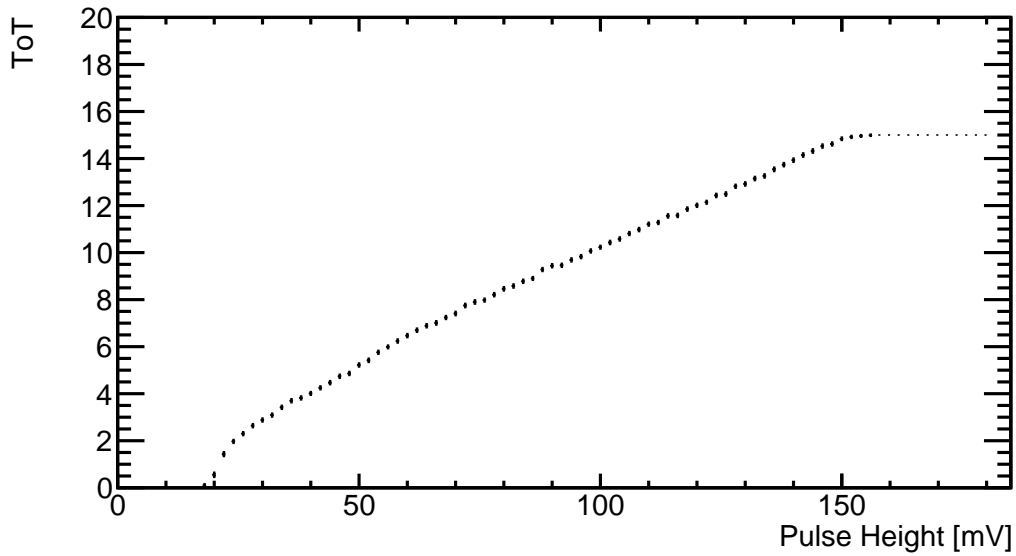


Figure 1.10: The CLICpix ToT as a function of injected pulse height. The black markers show the mean ToT and the error bars show the standard error.

Analysis

The functional form of the ToT against pulse height plot will be described using a surrogate function [2], which is defined as:

$$y = ax + b - \frac{c}{x - t}, \quad (1.1)$$

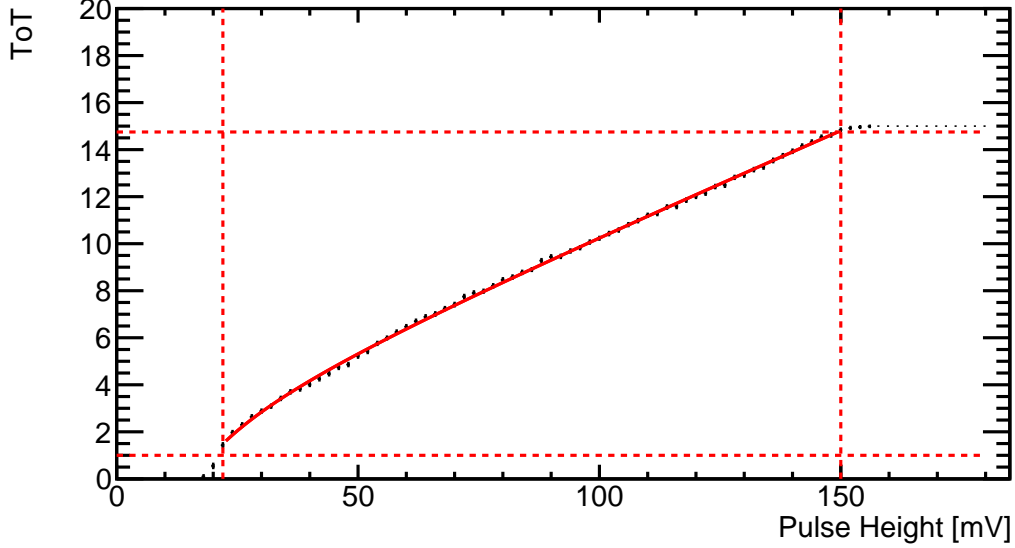


Figure 1.11: CLICpix ToT as a function of injected pulse height for a single pixel. The black markers are the mean ToT and the error bars are the standard error on the mean. The solid red line shows the surrogate function fit and the dotted red lines show the range where the fit was applied.

where y is the ToT, x is the pulse height in mV and a , b , c and t are fit parameters. Application of the fit helps to condense the large amount of data recorded for an individual pixel down to a small number of parameters, which makes categorisation of the response of the CLICpix matrix more clear. At large pulse heights the linear relationship dominates while for low pulse heights the inversely proportional term dominates. c describes the curvature of the graph, while t determines the asymptote below which no signal is detected. Figure 1.11 shows an example of the application of this fit. As this function does not describe saturation of the ToT or the region below threshold, the fit is only applied on data points where the mean ToT is greater than 1 and less than 14.75.

Results

A known issue with the design of the CLICpix ASIC is the unwanted feedback capacitance between the discriminator output and amplifier input. This feedback leads to an additional fixed injected charge being measured for each recorded hit, which means in effect that the chip operates at a higher-than-expected threshold. The magnitude of this effect differs between even and odd columns across the CLICpix matrix due

to slight differences in the physical layouts of alternating columns. By examining the distribution of the surrogate fit parameters, shown for SET9 in figure 1.12, this effect can be seen.

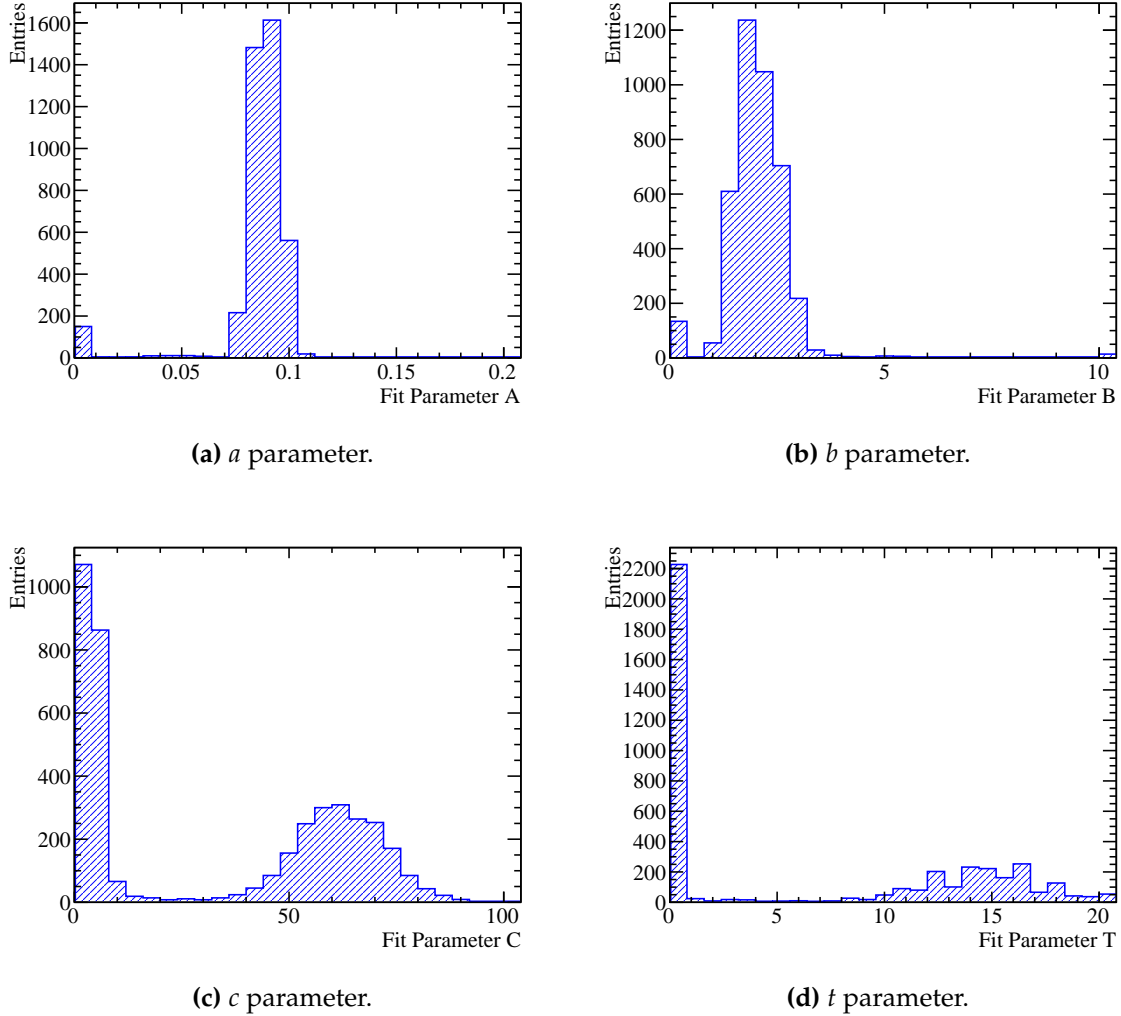


Figure 1.12: The distribution of the surrogate function parameters obtained when fitting the ToT as a function of injected pulse height for SET 9. (a), (b), (c) and (d) show the distribution of the a , b , c and d parameters respectively.

The peak at zero in the distribution of the a and b parameters, containing ≈ 150 entries, corresponds to noisy and dead pixels. These damaged pixels will be found in the device due to problems occurring in the manufacturing process. The majority of the a and b parameters are centred around a single value, which indicates a similar response in the linear region of the surrogate function, however, the c and t parameters are centred around one of two values. When examining the distribution of these

parameters as a function of position on the matrix, shown in figure 1.13 for a selected device, it can be seen that the structure is related to the column a given pixel is in. This feature is present in all devices considered and the underlying cause, the unwanted feedback capacitance, will be remedied in the next generation of the CLICpix ASIC.

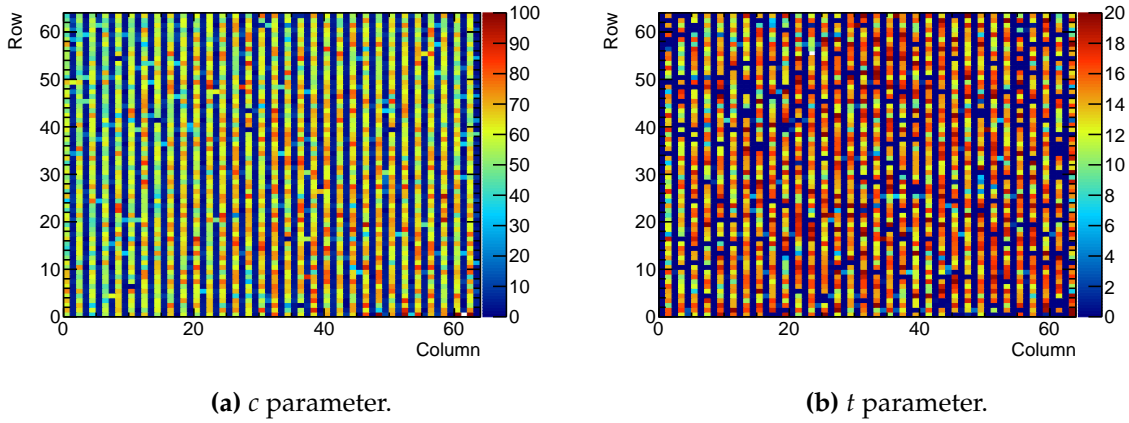


Figure 1.13: The distribution of selected surrogate function parameters obtained when fitting the ToT as a function of injected pulse height for SET 9 as a function of matrix position. (a) and (b) show the distribution of the c and t parameters respectively.

The matrix-averaged surrogate function fit parameters for all devices can be found in tables 1.2 and 1.3, for the even and odd columns respectively. The surrogate function for each device using these average parameters as input is shown in figure 1.14.

Assembly	a	b	c	t
SET 9	0.0875 ± 0.0005	2.41 ± 0.03	5.1 ± 0.1	12.79 ± 0.15
SET 10	0.0769 ± 0.0005	2.58 ± 0.03	7.5 ± 0.2	8.02 ± 0.14
SET 12	0.0725 ± 0.0005	2.87 ± 0.04	12.1 ± 0.3	7.86 ± 0.22
SET 13	0.0708 ± 0.0005	2.69 ± 0.03	16.2 ± 0.3	6.65 ± 0.18
SET 15	0.0856 ± 0.0005	2.34 ± 0.03	5.1 ± 0.2	12.51 ± 0.13
SET 16	0.0746 ± 0.0004	2.32 ± 0.02	13.7 ± 0.3	6.65 ± 0.16

Table 1.2: The average fit parameters for even columns of CLICpix sensor. The reported error was calculated using the standard error in the mean when averaging the fit parameters across the matrix.

As figure 1.14 shows, the response of the CLICpix to the injected pulse height is largely uniform across all samples. For all devices the turn-on pulse height is ≈ 10 mV

Assembly	a	b	c	t
SET 9	0.0834 ± 0.0003	1.72 ± 0.01	61.0 ± 0.3	0.25 ± 0.09
SET 10	0.0759 ± 0.0002	1.63 ± 0.01	43.2 ± 0.2	0.10 ± 0.02
SET 12	0.0731 ± 0.0003	1.92 ± 0.02	51.5 ± 0.3	0.36 ± 0.12
SET 13	0.0713 ± 0.0002	1.72 ± 0.01	52.5 ± 0.3	0.18 ± 0.07
SET 15	0.0836 ± 0.0003	1.52 ± 0.02	52.7 ± 0.3	0.42 ± 0.08
SET 16	0.0727 ± 0.0002	1.49 ± 0.01	50.7 ± 0.2	0.10 ± 0.03

Table 1.3: The average fit parameters for odd columns of CLICpix sensor. The reported error was calculated using the standard error in the mean when averaging the fit parameters across the matrix.

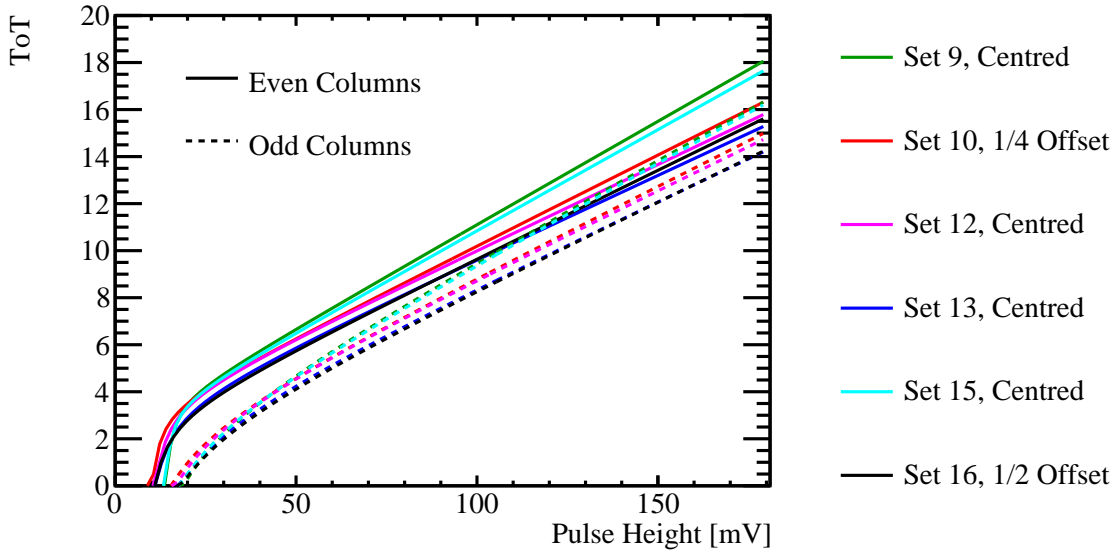


Figure 1.14: The average ToT response as a function of injected pulse height, which is represented using the surrogate function. Parameters for the surrogate function are obtained by fitting the ToT against pulse height curve for all pixels in the matrix. The results are divided into even and odd columns to account for the differing effective thresholds on alternate CLICpix columns.

and saturation, which occurs when the ToT output reaches the maximum value of 15, occurs at ≈ 150 mV. The differing column structure exists due to the unwanted feedback capacitance between the discriminator output and amplifier input. This unwanted feedback leads to a sharper rise in ToT for even-numbered columns than for odd-numbered columns, as in effect the even-numbered columns are operating at a lower threshold. This column structure is present in all devices considered.

The uniformity of the response of the CLICpix ASICs observed in this study make comparisons between the misaligned samples clearer. These results show that any performance differences observed between the misaligned devices do not originate from the intrinsic behaviour of the CLICpix ASIC.

1.4 Test Beam Analysis

To fully quantify the characteristics of the devices under consideration it is necessary to perform test beam measurements. Test beam measurements have an advantage over lab based measurements in that they give additional information relating to the properties of the particles passing through the device under test (DUT). This extends the descriptive power of the measurements that can be made in comparison to simple lab based measurements, in particular making efficiency calculations possible. This is of particular interest for this study as the efficiency of the device under realistic conditions will determine whether they are fit for use in the CLIC vertex detector.

The properties of particles passing through the DUT in the test beam setup will be measured using a telescope. In this context, a telescope consists of a number of planes of pixel detectors that are mounted either side of the DUT that will be used to map the trajectory of any particles passing through the DUT. It would, in principle, be possible to use a telescope to record the properties of the radioactive decay products used in the lab measurements, described in section 1.3.1. However, in practice, this would be extremely challenging as the radioactive decay products have so little energy that they would not be able to pass through the telescope to reach the DUT. Therefore, much higher particle energies than those found using radioactive sources are required for this measurement and such high energy particles can only be safely produced in a test beam experiment.

1.4.1 Test Beam Setup

The test beam experiments presented here were carried out in August and September 2015 on the H6 beam line in the CERN SPS North Area. The beam consisted of positively charged hadrons of momenta 120 GeV/c. Mean particle rates of 500 kHz/cm² were observed during the 4.8 s spills at intervals of 25 s. For the measurement the DUT were mounted on an EUDET/AIDA telescope [6]. This telescope consisted of

six planes of sensors, three on either side of the DUT, that used the Mimosa pixel technology. This telescope provided a resolution of $1.6\text{ }\mu\text{m}$ on the intercept position between tracks passing through the device and the DUT mounted on it.

1.4.2 Analysis

The track position on the DUT was calculated using the measured particle trajectory through the telescope planes. This was followed by a search around the intercept position on the DUT to find an associated cluster. Clusters were associated to the track if they fell within $75\text{ }\mu\text{m}$, or 3 pixels, about the intercept position. If multiple clusters were associated to a track the cluster position was calculated as the ToT-weighted centre-of-gravity. As tracks may undergo non-negligible multiple scattering, a χ^2 cut was used to remove less precisely reconstructed tracks. Pixels identified on the DUT that were deemed to be noisy were removed from the analysis. Any tracks with an intercept on the DUT within half a pixel width of a noisy pixel were also rejected from the analysis. A pixel was deemed noisy if it responded at a mean rate greater than 5σ in comparison to the average rate across the whole matrix. Finally, all tracks occurring within $125\text{ }\mu\text{m}$ of each other were vetoed, in order to reduce the possibility of mis-association of clusters to tracks.

Alignment of the telescope planes was essential for ensuring that the correct trajectory of the particles passing through the setup could be determined. Furthermore, alignment of the DUT with respect to the telescope planes is critical for ensuring the correct track intercept position was determined. With that in mind the six telescope planes were aligned by minimising the total track χ^2 with respect to the global alignment parameters. The tracks that are created in the alignment procedure are referred to as "rough tracks" as they are produced using the hits from sensor planes that may not be ideally aligned. The alignment proceeds one telescope plane at a time until all planes have been accounted for. This procedure is iteratively repeated, updating the global alignment parameters to the optimal values found each time, until no further gains can be made. Once the telescope planes have been aligned the DUT is aligned in a similar manor, but where the summed square of track residuals is minimised. The residual is defined as the difference between the track intercept and associated cluster centre-of-gravity.

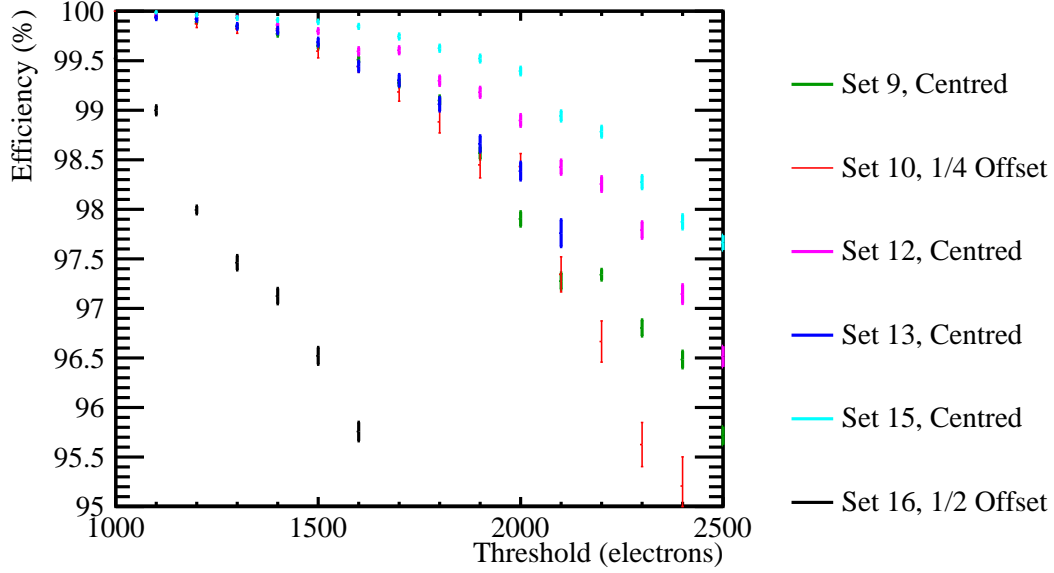


Figure 1.15: The efficiency of the devices considered as a function of the threshold applied.

1.4.3 Results

The metric used for characterising the device performance in the test beam is the single hit efficiency, ϵ . This is defined as the number of tracks with associated clusters recorded by the DUT, n , divided by the number of reconstructed tracks passing through the DUT recorded by the telescope, m . The errors shown on the efficiency measurements are given by $\sqrt{\frac{\epsilon(1-\epsilon)}{m}}$, which follows from the variance of n given binomial statistics with mean ϵ . The single hit efficiency as a function of threshold is shown in figure 1.15. The threshold, in units of number of electrons, is the size of the signal that must be injected into the CLICpix ASIC to generate a hit.

The data indicates that for all assemblies the single hit efficiency of the detector decreases when a higher amount of charge is required to generate a signal, which is to be expected. However, the efficiency of all samples, with the exception of the $\frac{1}{2}$ -offset sample, is still above 99% up to a threshold of 2000 electrons. This is encouraging behaviour as the larger the threshold that can be applied the lower the effects from noise will be. Reducing the effects from noise will aid tracking performance in the CLIC vertex detector, which is highly desirable. It is clear that the $\frac{1}{2}$ offset sample, SET 16, has a much lower efficiency as a function of threshold in comparison to the other samples. For the same deposited charge in the CCPDv3 the $\frac{1}{2}$ -offset sample will, due to the reduced capacitance, produce a smaller signal in the CLICpix than the centred

samples. This is the cause of the reduced efficiency as a function of threshold in this sample. More encouragingly is the behaviour of the $\frac{1}{4}$ -offset sample, SET 14, which in terms of performance is comparable to the aligned samples. There is a degradation in efficiency of the $\frac{1}{4}$ -offset sample with respect to the aligned sample, which is to be expected given the reduced capacitance, however, it is relatively small. These results indicate that even with a relatively large misalignment between the CCPDv3 and CLICpix pads the device performance is not significantly affected and, therefore, manufacturing tolerances of up to $\frac{1}{4}$ of a pixel width would not be problematic if this device were used for the CLIC vertex detector.

1.5 Conclusions

In summary, for the capacitively coupled pixel detectors considered in this analysis:

- The CCPDv3 sensor ASIC properties have been characterised and were found to be comparable across all devices.
- A calibration of the CLICpix readout ASIC was performed and their behaviour was found to be comparable across all devices.
- Combining the CCPDv3 and CLICpix characterisations it becomes clear that any performance differences between the devices are due to the capacitive coupling gluing layer as opposed to the intrinsic behaviour of the ASICs.
- Test beam analysis of the devices found that device fabrication tolerances of up to $\frac{1}{4}$ of a pixel width would not harm the performance of these devices should they be used for the CLIC vertex detector.

Colophon

This thesis was made in $\text{\LaTeX}2_\epsilon$ using the “hepthesis” class [\[4\]](#).

Bibliography

- [1] Roel Aaij, Bernardo Adeva, Marco Adinolfi, Ziad Ajaltouni, Simon Akar, Johannes Albrecht, Federico Alessio, Michael Alexander, Suvayu Ali, Georgy Alkhazov, Paula Alvarez Cartelle, Antonio Augusto Alves Jr, Sandra Amato, Silvia Amerio, Yasmine Amhis, Liupan An, Lucio Anderlini, Guido Andreassi, Mirco Andreotti, Jason Andrews, Mario Anelli, Robert Appleby, Flavio Archilli, Philippe d'Argent, Joan Arnau Romeu, Alexander Artamonov, Marina Artuso, Elie Aslanides, Giulio Auriemma, Marouen Baalouch, Igor Babuschkin, Sebastian Bachmann, John Back, Alexey Badalov, Clarissa Baesso, Sophie Baker, Vladislav Balagura, Wander Baldini, Alessandro Balla, Alexander Baranov, Roger Barlow, Colin Barschel, Sergey Barsuk, William Barter, Fedor Baryshnikov, Mateusz Baszczyk, Varvara Batozskaya, Baasansuren Batsukh, Vincenzo Battista, Aurelio Bay, Leo Beaucourt, John Beddow, Franco Bedeschi, Ignacio Bediaga, Andrew Beiter, Lennaert Bel, Violaine Bellee, Nicoletta Belloli, Konstantin Belous, Ivan Belyaev, Eli Ben-Haim, Giovanni Bencivenni, Sean Benson, Sarah Beranek, Alexander Berezhnoy, Roland Bernet, Alessandro Bertolin, Christopher Betancourt, Federico Betti, Marc-Olivier Bettler, Martinus van Beuzekom, Iaroslava Bezshyiko, Simone Bifani, Pierre Billoir, Alex Birnkraut, Alexander Bitadze, Andrea Bizzeti, Thomas Blake, Frederic Blanc, Johan Blouw, Steven Blusk, Valerio Bocci, Thomas Boettcher, Alexander Bondar, Nikolay Bondar, Walter Bonivento, Igor Bordyuzhin, Alessio Borgheresi, Silvia Borghi, Maxim Borisyak, Martino Borsato, Francesco Bossu, Meriem Boubdir, Themistocles Bowcock, Espen Eie Bowen, Concezio Bozzi, Svende Braun, Thomas Britton, Jolanta Brodzicka, Davide Brundu, Emma Buchanan, Christopher Burr, Albert Bursche, Jan Buytaert, Sandro Cadeddu, Roberto Calabrese, Marta Calvi, Miriam Calvo Gomez, Alessandro Camboni, Pierluigi Campana, Daniel Hugo Campora Perez, Lorenzo Capriotti, Angelo Carbone, Giovanni Carboni, Roberta Cardinale, Alessandro Cardini, Maurizio Carletti, Paolo Carniti, Laurence Carson, Kazuyoshi Carvalho Akiba, Gianluigi Casse, Lorenzo Cassina, Lucia Castillo Garcia, Luigi Casu, Marco Cattaneo, Giovanni Cavallero, Riccardo Cenci, David

Chamont, Matthew Charles, Philippe Charpentier, Georgios Chatzikonstantinidis, Maximilien Chefdeville, Shanzhen Chen, Shu-Faye Cheung, Veronika Chobanova, Marcin Chrzaszcz, Alexsei Chubykin, Paolo Ciambrone, Xabier Cid Vidal, Gregory Ciezarek, Mauro Citterio, Peter Clarke, Marco Clemencic, Harry Cliff, Joel Closier, Victor Coco, Simone Coelli, Julien Cogan, Eric Cogneras, Violetta Cogoni, Lucian Cojocariu, Paula Collins, Albert Comerma-Montells, Andrea Contu, Andrew Cook, George Coombs, Samuel Coquereau, Gloria Corti, Marco Corvo, Cayo Mar Costa Sobral, Benjamin Couturier, Greig Cowan, Daniel Charles Craik, Andrew Crocombe, Melissa Maria Cruz Torres, Samuel Cunliffe, Robert Currie, Carmelo D'Ambrosio, Franciole Da Cunha Marinho, Elena Dall'Occo, Jeremy Dalseno, Pieter David, Adam Davis, Kristof De Bruyn, Stefano De Capua, Michel De Cian, Jussara De Miranda, Leandro De Paula, Marilisa De Serio, Patrizia De Simone, Cameron Thomas Dean, Daniel Decamp, Mirko Deckenhoff, Luigi Del Buono, Moritz Demmer, Adam Dendek, Denis Derkach, Olivier Deschamps, Francesco Dettori, Biplab Dey, Angelo Di Canto, Pasquale Di Nezza, Hans Dijkstra, Francesca Dordei, Mirco Dorigo, Alvaro Dosil Suárez, Anatoliy Dovbnya, Karlis Dreimanis, Laurent Dufour, Giulio Dujany, Kevin Dungs, Paolo Durante, Rustem Dzhelyadin, Agnieszka Dziurda, Alexey Dzyuba, Nicolas D'Almeida, Sajan Easo, Marcus Ebert, Ulrik Egede, Victor Egorychev, Semen Eidelman, Stephan Eisenhardt, Ulrich Eitschberger, Robert Ekelhof, Lars Eklund, Scott Ely, Sevda Esen, Hannah Mary Evans, Timothy Evans, Antonio Falabella, Nathanael Farley, Stephen Farry, Robert Fay, Davide Fazzini, Giulietto Felici, Dianne Ferguson, Gerard Fernandez, Antonio Fernandez Prieto, Fabio Ferrari, Fernando Ferreira Rodrigues, Massimiliano Ferro-Luzzi, Sergey Filippov, Rosa Anna Fini, Marco Fiore, Massimiliano Fiorini, Mirosław Firlej, Conor Fitzpatrick, Tomasz Fiutowski, Frederic Fleuret, Klaus Fohl, Marianna Fontana, Flavio Fontanelli, Dean Charles Forshaw, Roger Forty, Vinicius Franco Lima, Markus Frank, Christoph Frei, Paolo Fresch, Jinlin Fu, Wolfgang Funk, Emiliano Furfaro, Christian Färber, Abraham Gallas Torreira, Domenico Galli, Stefano Gallorini, Silvia Gambetta, Miriam Gandelman, Paolo Gandini, Yuanning Gao, Luis Miguel Garcia Martin, Julián García-Pardiñas, Jordi Garra Tico, Lluís Garrido, Philip John Garsed, David Gascon, Clara Gaspar, Maurizio Gatta, Laura Gavardi, Giulio Gazzoni, David Gerick, Evelina Gersabeck, Marco Gersabeck, Timothy Gershon, Philippe Ghez, Sebastiana Gianáñ, Valerie Gibson, Olivier Gauran Girard, Lavinia-Helena Giubega, Konstantin Gizdov, Vladimir Gligorov, Dmitry Golubkov, Andrey Golutvin, Alvaro Gomes, Igor Vladimirovich Gorelov, Claudio Gotti, Ekaterina Govorkova, Ricardo Gra-

ciani Diaz, Luis Alberto Granado Cardoso, Eugeni GraugÀl's, Elena Graverini, Giacomo Graziani, Alexandru Grecu, Roman Greim, Peter Griffith, Lucia Grillo, Barak Raimond Gruberg Cazon, Oliver GrÀijnberg, Evgeny Gushchin, Yury Guz, Thierry Gys, Carla GÀúbel, Thomas Hadavizadeh, Christos Hadjivasiliou, Guido Haefeli, Christophe Haen, Susan Haines, Brian Hamilton, Xiaoxue Han, Stephanie Hansmann-Menzemer, Neville Harnew, Samuel Harnew, Jonathan Harrison, Mark Hatch, Jibo He, Timothy Head, Arno Heister, Karol Hennessy, Pierre Henrard, Louis Henry, Eric van Herwijnen, Miriam HeÀ§, AdlÀÁne Hicheur, Donal Hill, Christoph Hombach, P H Hopchev, Zachary Huard, Wouter Hulsbergen, Thibaud Humair, Mikhail Hushchyn, David Hutchcroft, Marek Idzik, Philip Ilten, Richard Jacobsson, Pawel Jalocho, Eddy Jans, Abolhassan Jawahery, Feng Jiang, Malcolm John, Daniel Johnson, Christopher Jones, Christian Joram, Beat Jost, Nathan Jurik, Sergii Kandybei, Matthias Karacson, James Mwangi Kariuki, Sarah Karodia, Matthieu Kecke, Matthew Kelsey, Matthew Kenzie, Tjeerd Ketel, Egor Khairullin, Basem Khanji, Chitsanu Khurewathanakul, Thomas Kirn, Suzanne Klaver, Konrad Klimaszewski, Tatsiana Klimkovich, Serhii Koliiev, Michael Kolpin, Ilya Komarov, Patrick Koppenburg, Alena Kosmyntseva, Sofia Kotriakhova, Anastasiia Kozachuk, Mohamad Kozeiha, Leonid Kravchuk, Katharina Kreplin, Michal Kreps, Pavel Krovovny, Florian Kruse, Wojciech Krzemien, Wojciech Kucewicz, Marcin Kucharczyk, Vasily Kudryavtsev, Axel Kevin Kuonen, Krzysztof Kurek, Tengiz Kvaratskheliya, Daniel Lacarrere, George Lafferty, Adriano Lai, Christoph Langenbruch, Thomas Latham, Cristina Lazzeroni, Renaud Le Gac, Jeroen van Leerdam, Alexander Leflat, Jacques LefranÀgois, Regis LefÀÁvre, Florian Lemaitre, Edgar Lemos Cid, Olivier Leroy, Tadeusz Lesiak, Blake Leverington, Tenglin Li, Yiming Li, Zhuoming Li, Tatiana Likhomanenko, Rolf Lindner, Federica Lionetto, Xuesong Liu, David Loh, Angelo Loi, Iain Longstaff, Jose Lopes, Donatella Lucchesi, Miriam Lucio Martinez, Haofei Luo, Anna Lupato, Eleonora Luppi, Oliver Lupton, Alberto Lusiani, Xiao-Rui Lyu, Frederic Machefert, Florin Maciuc, Oleg Maev, Kevin Maguire, Sneha Malde, Alexander Malinin, Timofei Maltsev, Giulia Manca, Giampiero Mancinelli, Peter Michael Manning, Jan Maratas, Jean FranÀgois Marchand, Umberto Marconi, Carla Marin Benito, Matthieu Marinangeli, Pietro Marino, JÀúrg Marks, Davide Marras, Giuseppe Martellotti, Morgan Martin, Maurizio Martinelli, Diego Martinez Santos, Fernando Martinez Vidal, Danielle Martins Tostes, Laure Marie Massacrier, AndrÀl Massafferri, Rosen Matev, Abhijit Mathad, Zoltan Mathe, Clara Matteuzzi, Andrea Mauri, Emilie Maurice, Brice Maurin, Alexander Mazurov, Michael McCann, Andrew McNab, Ronan McNulty, Brian Meadows,

Frank Meier, Dmytro Melnychuk, Marcel Merk, Andrea Merli, Emanuele Michielin, Diego Alejandro Milanes, Marie-Noelle Minard, Dominik Stefan Mitzel, Andrea Mogini, Josue Molina Rodriguez, Igancio Alberto Monroy, Stephane Monteil, Mauro Morandin, Piotr Morawski, Michael Joseph Morello, Olga Morgunova, Jakub Moron, Adam Benjamin Morris, Raymond Mountain, Franz Muheim, Mick Mulder, Manuel Mussini, Dominik M  ijller, Janine M  ijller, Katharina M  ijller, Vanessa M  ijller, Paras Naik, Tatsuya Nakada, Raja Nandakumar, Anita Nandi, Irina Nasteva, Matthew Needham, Nicola Neri, Sebastian Neubert, Niko Neufeld, Max Neuner, Thi Dung Nguyen, Chung Nguyen-Mau, Simon Nieswand, Ramon Niet, Nikolay Nikitin, Thomas Nikodem, Alla Nogay, Alexey Novoselov, Daniel Patrick O'Hanlon, Agnieszka Oblakowska-Mucha, Vladimir Obraztsov, Stephen Ogilvy, Rudolf Oldeman, Gerco Onderwater, Juan Martin Otalora Goicochea, Adam Otto, Patrick Owen, Maria Aranzazu Oyanguren, Preema Rennee Pais, Antimo Palano, Matteo Palutan, Antonios Papanestis, Marco Pappagallo, Luciano Pappalardo, Cheryl Pappenheimer, William Parker, Christopher Parkes, Giovanni Passaleva, Alessandra Pastore, Mitesh Patel, Claudia Patrignani, Alex Pearce, Antonio Pellegrino, Gianni Penso, Monica Pepe Altarelli, Stefano Perazzini, Pascal Perret, Luca Pescatore, Konstantinos Petridis, Alessandro Petrolini, Aleksandr Petrov, Marco Petruzzo, Eduardo Picatoste Olloqui, Boleslaw Pietrzyk, Malgorzata Pikies, Davide Pinci, Alessandro Pistone, Alessio Piucci, Vlad-Mihai Placinta, Stephen Playfer, Maximo Plo Casasus, Tuomas Poikela, Francesco Polci, Marco Poli Lener, Anton Poluektov, Ivan Polyakov, Erica Polycarpo, Gabriela Johanna Pomery, Sebastien Ponce, Alexander Popov, Dmitry Popov, Bogdan Popovici, Stanislav Poslavskii, C  ldric Potterat, Eugenia Price, Jessica Prisciandaro, Claire Prouve, Valery Pugatch, Albert Puig Navarro, Giovanni Punzi, Chen Qian, Wenbin Qian, Renato Quagliani, Bartolomiej Rachwal, Jonas Rademacker, Matteo Rama, Miguel Ramos Pernas, Murilo Rangel, Iurii Raniuk, Fedor Ratnikov, Gerhard Raven, Federico Redi, Stefanie Reichert, Alberto dos Reis, Clara Remon Alepuz, Victor Renaudin, Stefania Ricciardi, Sophie Richards, Mariana Rihl, Kurt Rinnert, Vicente Rives Molina, Patrick Robbe, Ana Barbara Rodrigues, Eduardo Rodrigues, Jairo Alexis Rodriguez Lopez, Pablo Rodriguez Perez, Alexey Rogozhnikov, Stefan Roiser, Alexandra Paige Rollings, Vladimir Romanovski, Antonio Romero Vidal, John William Ronayne, Marcello Rotondo, Matthew Scott Rudolph, Thomas Ruf, Pablo Ruiz Valls, Juan Jose Saborido Silva, Elnur Sadykhov, Naylya Sigidova, Biagio Saitta, Valdir Salustino Guimaraes, David Sanchez Gonzalo, Carlos Sanchez Mayordomo, Brais Sanmartin Sedes, Roberta Santacesaria, Cibr  n Santa-

marina Rios, Marco Santimaria, Emanuele Santovetti, Alessandro Saputi, Alessio Sarti, Celestina Satriano, Alessia Satta, Daniel Martin Saunders, Darya Savrina, Stefan Schael, Margarete Schellenberg, Manuel Schiller, Heinrich Schindler, Maximilian Schlupp, Michael Schmelling, Timon Schmelzer, Burkhard Schmidt, Olivier Schneider, Andreas Schopper, HF Schreiner, Konstantin Schubert, Maxime Schubiger, Marie Helene Schune, Rainer Schwemmer, Barbara Sciascia, Adalberto Sciubba, Alexander Semennikov, Antonino Sergi, Nicola Serra, Justine Serrano, Lorenzo Sestini, Paul Seyfert, Mikhail Shapkin, Illya Shapoval, Yury Shcheglov, Tara Shears, Lev Shekhtman, Vladimir Shevchenko, Benedetto Gianluca Siddi, Rafael Silva Coutinho, Luiz Gustavo Silva de Oliveira, Gabriele Simi, Saverio Simone, Marek Sirendi, Nicola Skidmore, Tomasz Skwarnicki, Eluned Smith, Iwan Thomas Smith, Jackson Smith, Mark Smith, Lais Soares Lavra, Michael Sokoloff, Paul Soler, Bruno Souza De Paula, Bernhard Spaan, Patrick Spradlin, Srikanth Sridharan, Federico Stagni, Marian Stahl, Sascha Stahl, Pavol Stefko, Slavomira Stefkova, Olaf Steinkamp, Simon Stemmler, Oleg Stenyakin, Holger Stevens, Sabin Stoica, Sheldon Stone, Barbara Storaci, Simone Stracka, Maria Elena Stramaglia, Mihai Straticiuc, Ulrich Straumann, Liang Sun, William Sutcliffe, Krzysztof Swientek, Vasileios Syropoulos, Marek Szczekowski, Tomasz Szumlak, Stephane T'Jampens, Andrey Tayduganov, Tobias Tekampe, Giulia Tellarini, Frederic Teubert, Eric Thomas, Jeroen van Tilburg, Matthew James Tilley, Vincent Tisserand, Mark Tobin, Siim Tolk, Luca Tomassetti, Diego Tonelli, Stig Topp-Joergensen, Francis Toriello, Rafael Tourinho Jadallah Aoude, Edwige Tournier, Stephane Tourneur, Karim Trabelsi, Murdo Traill, Minh T'Ácm Tran, Marco Tresch, Ana Trisovic, Andrei Tsaregorodtsev, Panagiotis Tsopelas, Alison Tully, Niels Tuning, Artur Ukleja, Andrey Ustyuzhanin, Ulrich Uwer, Claudia Vacca, Vincenzo Vagnoni, Andrea Valassi, Sebastien Valat, Giovanni Valenti, Maarten Van Dijk, Ricardo Vazquez Gomez, Pablo Vazquez Regueiro, Stefania Vecchi, Maarten van Veghel, Jaap Velthuis, Michele Veltri, Giovanni Veneziano, Aravindhavan Venkateswaran, Tobias Anton Verlage, Maxime Vernet, Mika Vesterinen, Joao Vitor Viana Barbosa, Benoit Viaud, Daniel Vieira, Maria Vieites Diaz, Harald Viemann, Xavier Vilasis-Cardona, Marcela Vitti, Vladimir Volkov, Achim Vollhardt, Balazs Voneki, Alexey Vorobyev, Vitaly Vorobyev, Christian Voß, Jacco de Vries, Carlos Vázquez Sierra, Roland Waldi, Charlotte Wallace, Ronan Wallace, John Walsh, Jianchun Wang, David Ward, Heather McKenzie Wark, Nigel Watson, David Websdale, Andreas Weiden, Mark Whitehead, Jean Wicht, Guy Wilkinson, Michael Wilkinson, Mark Richard James Williams, Matthew Williams, Mike Williams, Tim-

- othy Williams, Fergus Wilson, Jack Wimberley, Michael Andreas Winn, Julian Wishahi, Wojciech Wislicki, Mariusz Witek, Guy Wormser, Stephen Wotton, Kenneth Wraight, Kenneth Wyllie, Yuehong Xie, Zhou Xing, Zhirui Xu, Zhenwei Yang, Zishuo Yang, Yuezhe Yao, Hang Yin, Jiesheng Yu, Xuhao Yuan, Oleg Yushchenko, Kristian Alexander Zarebski, Mikhail Zavertyaev, Liming Zhang, Yanxi Zhang, Alexey Zhelezov, Yangheng Zheng, Xianglei Zhu, Valery Zhukov, and Stefano Zucchelli. Expression of Interest for a Phase-II LHCb Upgrade: Opportunities in flavour physics, and beyond, in the HL-LHC era. Technical Report CERN-LHCC-2017-003, CERN, Geneva, Feb 2017.
- [2] Niloufar Alipour Tehrani, Samir Arfaoui, Mathieu Benoit, Damiano Celeste, Dominik Dannheim, Florentina Pfleger, and Sophie Redford. Calibration of ultra-thin hybrid pixel detector assemblies with Timepix readout ASICs. Sep 2015.
- [3] M. Benoit et al. Testbeam results of irradiated ams H18 HV-CMOS pixel sensor prototypes. 2016, 1611.02669.
- [4] Andy Buckley. The hepthesis \LaTeX class.
- [5] A Dominguez, D Abbaneo, K Arndt, N Bacchetta, A Ball, E Bartz, W Bertl, G M Bilei, G Bolla, H W K Cheung, M Chertok, S Costa, N Demaria, Daniel Dominguez Vazquez, K Ecklund, W Erdmann, K Gill, G Hall, K Harder, F Hartmann, R Horisberger, W Johns, H C Kaestli, K Klein, D Kotlinski, S Kwan, M Pesaresi, H Postema, T Rohe, C SchÃd'fer, A Starodumov, S Streuli, A Tricomi, P Tropea, J Troska, F Vasey, and W Zeuner. CMS Technical Design Report for the Pixel Detector Upgrade. Technical Report CERN-LHCC-2012-016. CMS-TDR-11, Sep 2012. Additional contacts: Jeffrey Spalding, Fermilab, Jeffrey.Spalding@cern.ch Didier Contardo, Universite Claude Bernard-Lyon I, didier.claude.contardo@cern.ch.
- [6] I Rubinskiy. An EUDET/AIDA Pixel Beam Telescope for Detector Development. (AIDA-CONF-2015-035), Jun 2011.

List of figures

1.1	Schematic cross section of an HV-CMOS sensor: the deep n-well is the charge-collecting electrode and also contains additional CMOS circuits such as a preamplifier. Image taken from [3].	3
1.2	Schematic cross section of an n-MOS transistor. p-MOS transistors have a similar cross section where the n and p doped regions are switched. .	3
1.3	Schematic of CCPDv3 and CLICpix pixels.	5
1.4	Alignment schematic of the CCPDv3 and CLICpix detectors studied. The red dotted line represents the CCPDv3 pad and the solid black line represents the CLICpix top metal layer. From left to right; centred pixels, 1/4 offset (6.25 μm) and 1/2 offset (12.5 μm).	7
1.5	CCPDv3 voltage pulses produced using a radioactive source, Sr^{90} , to deposit charge in the sensor.	9

1.6	An example calculation of the pulse height and rise time for the CCPDv3 output voltage. In this example the black line show the CCPDv3 output voltage as a function of time where the baseline voltage has been subtracted and the pulse shape inverted. These voltage pulses were created using a radioactive source, Sr^{90} , to deposit charge in the sensor. (a) The definition of the pulse height. Pulse height is defined as the amplitude of a Gaussian function fitted across the peak of the voltage pulse. The peak of the voltage pulse is defined as the region where the voltage in excess of 90% of the raw pulse height, which is indicated in the figure by the red arrow. The red dotted line shows the Gaussian fit used to extract the pulse height. (b) The definition of rise time. Rise time is defined as the time taken for the CCPDv3 voltage to rise from 10% to 90% of the raw pulse height. The rise time, and change in CCPDv3 output voltage over this time, are shown in the figure by the blue arrows.	11
1.7	The CCPDv3 output voltage rise time as a function of pulse height. . .	12
1.8	The mean ToT measured on the CLICpix ASIC as a function of CCPDv3 voltage pulse height.	13
1.9	The mean ToT measured on the adjacent CLICpix pixel, along the direction of the offset, as a function of CCPDv3 voltage pulse height for (a) the centred and (b) the misaligned devices.	14
1.10	The CLICpix ToT as a function of injected pulse height. The black markers show the mean ToT and the error bars show the standard error.	16
1.11	CLICpix ToT as a function of injected pulse height.	17
1.12	The distribution of the surrogate function parameters obtained when fitting the ToT as a function of injected pulse height for SET 9. (a), (b), (c) and (d) show the distribution of the a , b , c and d parameters respectively.	18
1.13	The distribution of selected surrogate function parameters obtained when fitting the ToT as a function of injected pulse height for SET 9 as a function of matrix position. (a) and (b) show the distribution of the c and t parameters respectively.	19

1.14 The average ToT response as a function of injected pulse height, which is represented using the surrogate function. Parameters for the surrogate function are obtained by fitting the ToT against pulse height curve for all pixels in the matrix. The results are divided into even and odd columns to account for the differing effective thresholds on alternate CLICpix columns.	20
1.15 The efficiency of the devices considered as a function of the threshold applied.	23

List of tables

1.1	A list detailing the alignment of the CCPDv3 and CLICpix coupling pads for the devices considered in this study.	7
1.2	The average fit parameters for even columns of CLICpix sensor. The reported error was calculated using the standard error in the mean when averaging the fit parameters across the matrix.	19
1.3	The average fit parameters for odd columns of CLICpix sensor. The reported error was calculated using the standard error in the mean when averaging the fit parameters across the matrix.	20